Article

Characterization of Fluid Flow and Heat Transfer of Expanded Metal Meshes for Catalytic Processes

Marzena Iwaniszyn [1,*], Katarzyna Sindera [1], Anna Gancarczyk [1], Bartosz Leszczyński [2], Mateusz Korpyś [1], Mikołaj Suwak [1], Andrzej Kołodziej [1,3] and Przemysław J. Jodłowski [4]

1. Institute of Chemical Engineering, Polish Academy of Sciences, Bałtycka 5, 44-100 Gliwice, Poland
2. M. Smoluchowski Institute of Physics, Jagiellonian University, Prof. Stanisława Łojasiewicza 11, 30-348 Kraków, Poland
3. Faculty of Civil Engineering and Architecture, Opole University of Technology, Katowicka 48, 45-061 Opole, Poland
4. Faculty of Chemical Engineering and Technology, Kraków University of Technology, Warszawska 24, 31-155 Kraków, Poland
* Correspondence: miwaniszyn@iich.gliwice.pl

Abstract: In this work, three raised expanded metal meshes (EMMs) differing in mesh size were tested experimentally with regard to their flow and transport properties. Empirical equations for the Nusselt number and Fanning friction factor were developed. Alongside the experiments, simple computational fluid dynamics (CFD) models were used to simulate the pressure drop and heat transfer coefficients within EMMs. Finally, the Performance Efficiency Criterion (PEC) was applied to compare EMMs with other reactor packings.

Keywords: heat transfer; flow resistance; expanded metal mesh; structured reactor; CFD modelling

1. Introduction

The design and optimization of structured reactors' performance are crucial for environmental catalytic processes such as the catalytic combustion of volatile organic compounds (VOCs) or the selective catalytic reduction (SCR) of nitrogen oxides (NOx). It is highly desirable to ensure a large surface-area-to-volume ratio and high heat and mass transfer rates to maximize the catalyst consumption and, at the same time, low flow resistance to reduce pumping costs [1,2]. Although significant progress in catalysis has been made, there is still a need to intensify the heat/mass transfer for catalytic reactors to ensure the overall process rate of faster reaction kinetics is not limited.

An effective technique to improve the rate of heat transfer to fluid flowing in a duct, as well as the rate of mass transfer of reagents to the catalyst surface, is the enhancement of fluid mixing. It can be obtained by applying a certain type of catalyst support, which provides some disarray in the flow. However, it would result in an increase in pressure drop. In order to keep the flow resistance at a minimum level, the mixing flow should exist in a region very close to the wall surface of the catalyst carrier.

Many different reactor fillings have been proposed to achieve the above phenomenon. Short-channel structures, which are short monoliths, are the simplest example due to the possibility of modifying their geometry (the ratio of the channel diameter to its length), as well as their arrangement in the reactor (alternating and/or with gaps) [3–6]. Solid foams ensure mixing flow, thus enhancing heat/mass transfer and low flow resistance, due to their stochastic structure [7–13]. The geometry of periodic open cellular structures is, in some sense, the combination of a foam matrix and a monolith structure, hence they are expected to enable fluid mixing [14,15].

Meshes, called also screens or grids, have been used for years to control fluid motion, thus it is possible to influence the direction, speed, or turbulence intensity of the flow [16,17].

Kołodziej et al. [18] investigated knitted and woven wire gauzes because of their wire arrangement. It was proven that gauzes enhance heat/mass transfer with a slight increase in flow resistance. In comparison with other available catalyst supports, gauze seems to be more efficient [7,19–22].

The expanded metal mesh (EMM) is a metal foil that is simultaneously slit and stretched longitudinally into a network of diamond- or hexagonal-shaped holes of uniform size, shape, and regularity [16,17,23]. It comes in four basic types: Raised (or standard), flattened, Gridwalk, and architectural (or decorative) meshes. EMM's applications include energy absorption, construction, protection–decoration, flow control, filtration, biomechanics, and electrochemical applications [17,24]. Expanded metal meshes are produced from a solid sheet or a plate. Carbon, aluminum, or stainless steel and different alloys including copper, nickel, silver, titanium, etc., can be used as materials. No metal is lost in the expanding process. After the process of cutting and plastic deformation, the area of the EMM is up to 12 times larger and its weight is reduced by 80% per square meter in comparison with the original sheet or plate [17,25]. The final product is much stiffer and more durable and has solid joints and no seams or welds. Because it is made from a solid sheet of metal, it can never untangle. Even if cut at one or more points, the remaining strand intersections continue to hold.

The flow behavior and its impact on heat transfer and flow resistance around expanded meshes have been studied by several researchers. Saini and Saini [26] experimentally investigated the turbulent flow in an artificially roughened rectangular duct with a large aspect ratio with an expanded metal mesh as the roughness element. The authors concluded that the use of an expanded metal mesh on the absorber plate of a solar air-heater duct brings the enhancement of heat transfer, depending on the system and operating parameters. The correlations for the Nusselt number and friction factor for the system were also developed. Oshinowo and Kuhn [17] performed an experimental study of the turbulent flow in a low-turbulence wind tunnel with expanded metal screens. The characteristics of mean velocity, pressure drop, and turbulence of expanded metal sheets were shown. Mustaffar et al. [24] experimentally and numerically tested the melting of the phase-change material (PCM) via a raised aluminum expanded metal mesh. It was shown that the presence of expanded metal meshes increased the PCM's effective thermal conductivity, resulting in a reduction in melting time. Mallick and Thombre [27] evaluated the performance of the passive direct methanol fuel cell (DMFC) and compared it with different combinations of supporting plates and an expanded metal mesh current collector (EMCC). It was found that better results were achieved for the passive DMFC with EMCC, which also facilitates a better distribution of the fuel on the anode catalyst layer and increases the operating temperature. Lafmejani et al. [25] experimentally and numerically studied the application of expanded metal meshes as flow plates in polymer electrolyte membrane (PEM) water electrolysis cells. It was shown, in particular, that the expanded metal grid behaves as a porous medium although there is a local flow of mixing. The authors measured the pressure loss under different orientations and velocities and found the dependence of measured parameters on the flow direction and size of the pores.

In this work, the internal fluid flow and heat transfer performance of raised expanded metal meshes differing in mesh openings was investigated experimentally and numerically. The effect of mesh geometry and dimensions on flow friction and heat-transfer characteristics in expanded metal grids was analyzed. New empirical equations of Fanning friction factors and Nusselt numbers were developed based on the experimental data. The results achieved for expanded metal screens were compared with packed bed, monolith, and woven wire gauzes in relation to the heat/mass transfer and flow resistance.

2. Materials and Methods

2.1. Expanded Meshes Characterization

Three types of expanded meshes made of stainless steel were tested. Figure 1 shows the structures of the expanded meshes, while Figure 2 and Table 1 present the mesh

characterization. The specific surface area (S_v) and the void fraction (ε) were determined based on scans from microtomography, while the other parameters were measured.
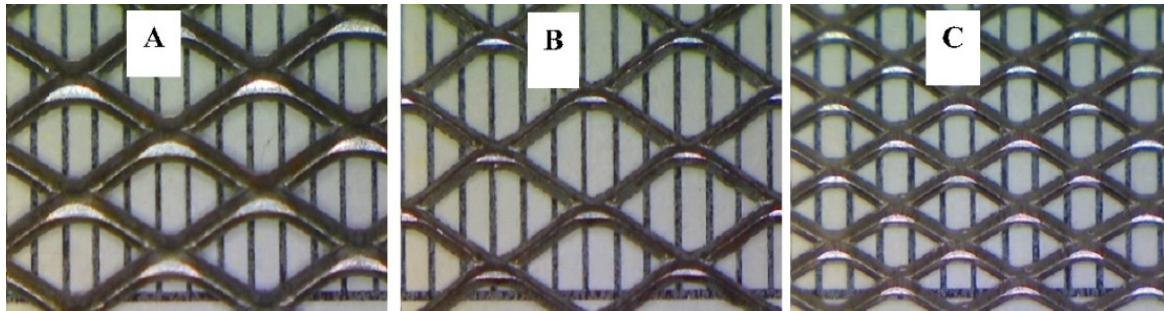

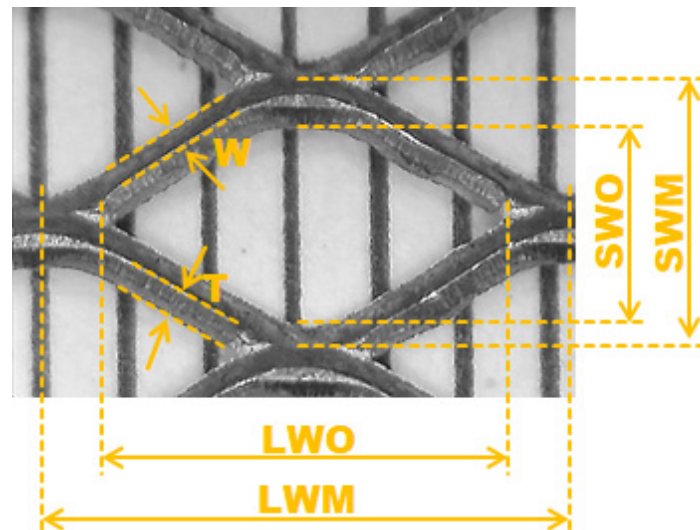**Figure 1.** Photos of single expanded meshes (**A–C**).

Figure 2. Mesh characterization.

Table 1. Geometrical parameters of expanded meshes.

Mesh Characterization	A	B	C
Length of mesh, LWM [mm]	6 (6 *)	6 (5 *)	4 (4 *)
Width of mesh, SWM [mm]	3.4 (3.4 *)	3.5 (3.5 *)	2.5 (2 *)
Length of opening, LWO [mm]	4 (4 *)	4.5 (3 *)	2 (2 *)
Width of opening, SWO [mm]	2 (2 *)	2.5 (2 *)	1.5 (1.5 *)
Strand thickness, T [mm]	0.5 (0.5 *)	0.4 (0.5 *)	0.3 (0.5 *)
Strand width, W [mm]	0.6 (0.6 *)	0.5 (0.5 *)	0.4 (0.6 *)
Sheet thickness, S [mm]	1.1	1	0.65
Specific surface area, S_v [m^2/m^3]	1100	900	1700
Void fraction, ε	0.84	0.9	0.84
Bed length, *L* [m]	0.0295	0.031	0.0181
Supplier	Ann-Filters Poland	Ann-Filters Poland	NETex-POL

* According to the supplier.

2.2. Experimental Procedure

The experimental apparatus applied for the pressure difference (A) and heat convection (B) measurements is shown schematically in Figure 3. A square reactor (30 × 30 mm) was employed to carry out the flow resistance experiments. Sheets of expanded meshes were placed inside the reactor without separating gaps. Table 1 shows the bed length *L*

of the sheets. The pressure drop was measured using the Recknagel micromanometer and water U-tube manometer. The flow resistance experiments were performed for gas velocities u_0 of $0.07 \div 4$ m/s at room temperature and ambient pressure.
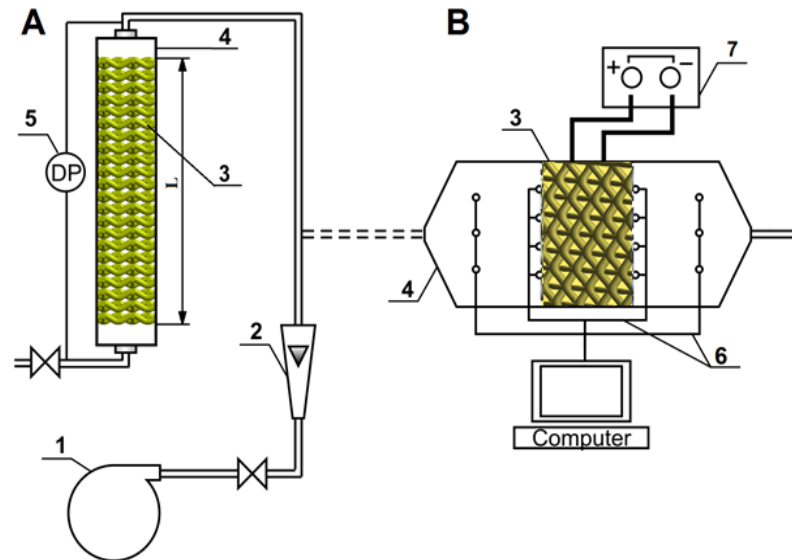

Figure 3. Experimental apparatus for pressure drop (**A**) and heat transfer (**B**) measurements: 1—blower; 2—flowmeter; 3—wire gauze; 4—test reactor; 5—manometer; 6—thermocouples; 7—electric current.

A test reactor with a rectangular cross-section (45×30 mm) was used to perform the heat transfer experiments. A single expanded mesh was placed inside the reactor and heated by an electric current flowing directly through it. The inlet and outlet temperatures of the flowing air and mesh surface were measured with K-type thermocouples: Three thermocouples each at the reactor's inlet and outlet and four on the mesh surface on the inlet and outlet sides. Special composite glue that secured good heat conduction and no electric conduction was used to attach the thermocouples to the wire surface. The setup was connected to a computer data-acquisition system. Experiments were conducted with various superficial velocities of air u_0 entering the test section ($0.2 \div 3$ m/s).

2.3. Numerical Simulation

2.3.1. Computational Domain and Mesh Generation

The commercial code ANSYS FLUENT 21.2, based on the finite volume method, was employed as a CFD tool. The geometry models were created to simplify the meshing procedure. The domain was discretized with a high-quality mesh and tetrahedral cells in the core of the domain, while 5 prism layers were implemented near the mesh surface to collect the heat exchange between the mesh wall and the fluid. The detailed computational domain for mesh type B is shown in Figure 4.

The sensitivity analysis of the base size of the cells applied in the core of the domain, as well as on the heated wall, was carried out for each mesh type. Table 2 shows the variation of the unit pressure drop $\Delta P/L$ and Nusselt number Nu for $u_0 = 1$ m/s with respect to the number of elements for mesh type B. Finally, the fine grid was chosen for mesh type B, as well as for other meshes.
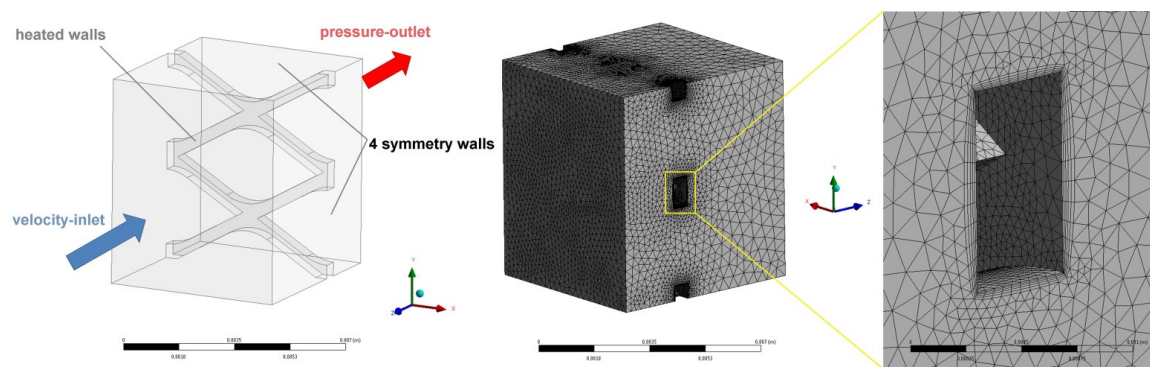
Figure 4. Computational domain for mesh type B with boundary conditions (**left**) and numerical grid (**right**).

Table 2. Grid independency results for mesh type B.

Grid Size	No. of Elements	$\Delta P/L$ [Pa/m]	Difference [%]	Nu	Difference [%]
Coarse	520,239	1952.06	2.5	58.3	0.87
Medium	766,915	1928.66	1.3	58.0	0.35
Fine	1,038,352	1903.90	-	57.8	-

2.3.2. Governing Equations

The continuity, momentum, and energy equations for the fluid phase are as follows:

$$\frac{\partial(\rho u_i)}{\partial x_i} = 0, \tag{1}$$

where ρ is the density, x_i is the Cartesian coordinates, and u_i is the velocity components.

$$\frac{\partial(\rho u_i u_j)}{\partial x_j} = -\frac{\partial p}{\partial x_i} + \frac{\partial \tau_{ij}}{\partial x_j}, \tag{2}$$

where p is the static pressure and τ_{ij} is the stress tensor.

$$\frac{\partial(\rho c_p u_i T)}{\partial x_j} = k\frac{\partial^2 T}{\partial x_j^2}, \tag{3}$$

where c_p is the specific heat, k is the thermal conductivity, and T is the temperature.

2.3.3. Boundary Conditions

All simulations were performed for the following boundary conditions:

- Velocity-inlet condition with a uniform value and a static temperature equal to 300 K was defined at the inlet.
- Pressure-outlet condition with zero-gauge pressure was defined at the outlet.
- Constant heat flux and no-slip conditions were imposed on the mesh surface.
- Symmetry condition on the four side boundaries of the computational domain.

2.3.4. Numerical Assumptions

The operation conditions for the simulation are as follows:

- The air is defined as an ideal gas.
- The flow is in the steady state and laminar due to the maximum value of the Reynolds number, which is nearly 1100 for the arrangement with mesh type B.
- The physical properties of the fluid phase are temperature dependent because of its variations in the simulations.

- The radiative effects were not considered.

2.3.5. Computational Methodology

- A commercially available CFD code, ANSYS FLUENT 21.2, was employed to simulate the fluid flow and heat transfer. The simulation procedure was:
- The pressure–velocity coupling formulation was handled with a coupled algorithm.
- The second-order upwind schemes of discretization were adopted for the momentum and energy equations.
- The residual limit was set to 1×10^{-3} for the continuity and momentum equations and 1×10^{-6} for the energy equation.

3. Results and Discussion

3.1. Flow Resistance

According to Saini and Saini [26], the Fanning friction factor f is calculated based on the pressure loss across the channel and air velocity, defined by the Darcy–Weisbach equation:

$$f = \frac{\Delta P}{L} \frac{\varepsilon^2 D_h}{2\rho u_0^2},$$ (4)

and presented as a function of the Reynolds number Re defined with the hydraulic diameter $D_h = 4\varepsilon/S_v$ and the interstitial fluid velocity $u_0 = u/\varepsilon$:

$$Re = \frac{\rho u_0 D_h}{\varepsilon \mu},$$ (5)

Figure 5 shows the flow resistance characteristics derived from experiments and numerical modeling for all three expanded meshes tested. It is noticeable for all EMMs that the higher the superficial gas velocity, the greater the unit pressure drop (Figure 5 left). The discrepancies in the unit pressure drop between different EMMs also increased. It should be noted that mesh type B indicates the lowest flow resistance, while mesh type C has the highest one. The comparison of experimental and numerical results indicates good agreement; the average relative error e_y is approximately 17.4%, 5.7%, and 18.2% for mesh types A, B, and C, respectively. The Fanning friction factor (Figure 5 right) for all meshes studied decreases when the Reynolds number increases, becoming flatter and flatter. However, the lower the Reynolds number, the smaller the discrepancies between meshes types. Computational simulations confirm this trend.
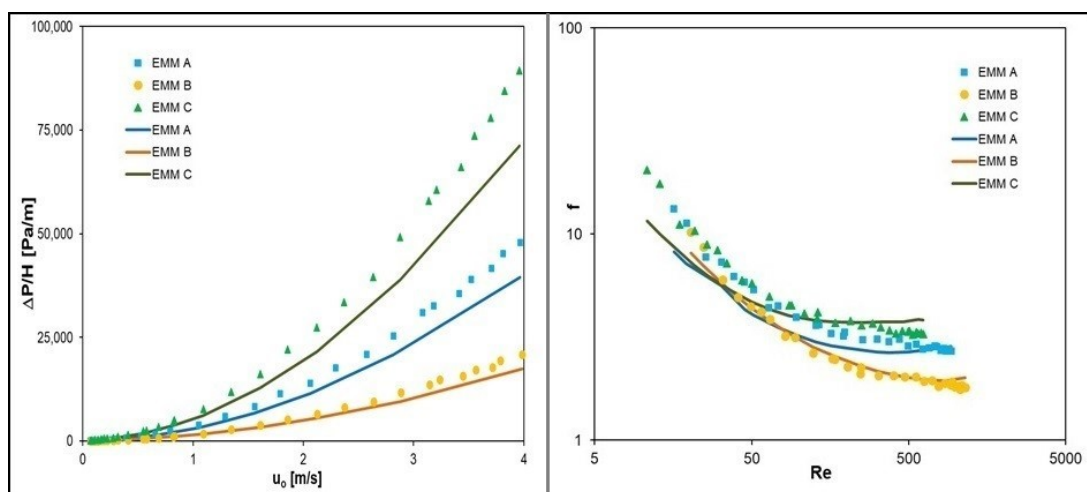

Figure 5. Flow resistance characteristics derived from experiments (points) and modeling (lines): (**left**)—unit pressure drop vs. superficial gas velocity; (**right**)—Fanning friction factor vs. Reynolds number.

The available literature relating to the expanded mesh does not propose correlations describing the flow resistance. Therefore, new formulae were developed (see Table 3) in the form of the Ergun [28] model:

$$f = \frac{A}{Re} + B, \tag{6}$$

where A and B differ for meshes. The fit of the developed equations to the experimental data is shown in Figure 6.

Table 3. Correlations for Fanning friction factors of expanded metal meshes.

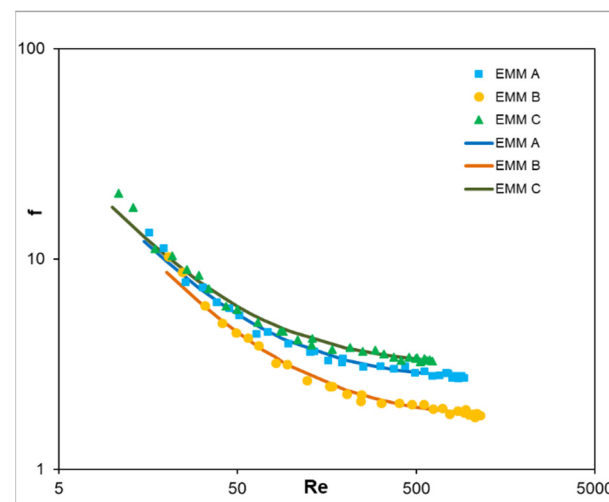| EMM	Correlation	Correlation Factor R^2	Difference [%]	No of Exp. Points
A	$f = \frac{131.82}{Re} + 2.4$	0.9988	3.07	30
B	$f = \frac{138.05}{Re} + 1.7$	0.9983	3.35	30
C	$f = \frac{144.56}{Re} + 3.1$	0.9987	3.95	30

Figure 6. Comparison of Fanning friction factor derived from experiments (points) and calculated by correlations from Table 3 (lines).

3.2. Heat Transfer

The Nusselt number Nu calculated from the heat transfer coefficient h is used to evaluate the heat transfer characteristic:

$$Nu = \frac{hD_h}{k}, \tag{7}$$

$$h = \frac{q}{F\Delta T}, \tag{8}$$

where ΔT is the logarithmic mean temperature difference between the mesh wall and the air at the inlet and outlet sides. The Nusselt number Nu is presented as a function of the Reynolds number Re.

Figure 7 presents the heat transfer results derived from experimental data and computational simulations for all EMMs tested. It is visible for all meshes that the higher the superficial gas velocity, the greater the heat transfer coefficients (Figure 7 left). It should be noted that mesh type B indicates the most intense heat transfer, while the heat transfer characteristics for mesh types A and C are located close together. Similar results were achieved using CFD modeling. The comparison of experimental and numerical results indicates that CFD modelling is able to predict the heat transfer of expanded metal meshes with reasonable accuracy (the average relative error e_y is approximately 10.1%, 22.3%, and 14.7 for mesh types A, B, and C, respectively).
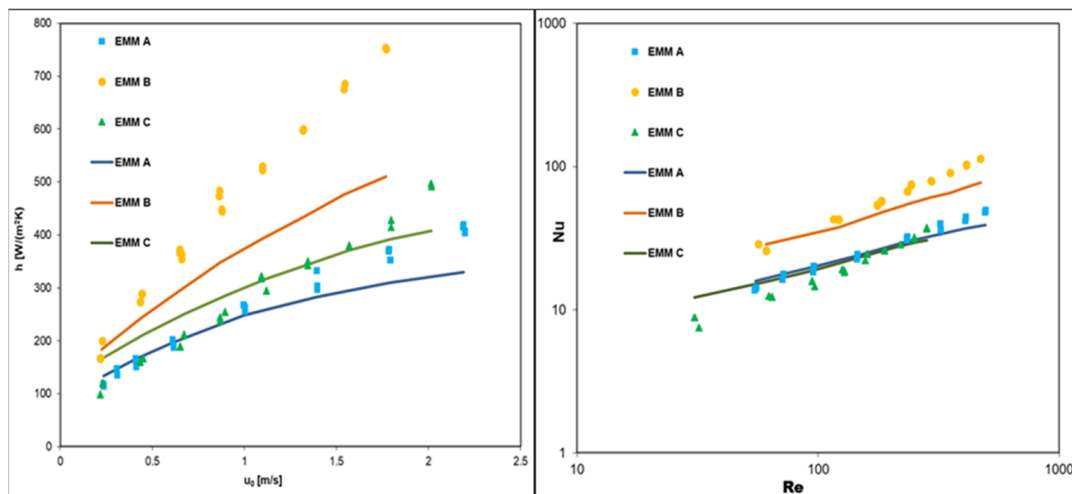
Figure 7. Heat transfer characteristics derived from experiments (points) and modeling (lines): left—heat transfer coefficient vs. superficial gas velocity; right—Nusselt number vs. Reynolds number.

The available literature relating to the expanded mesh does not propose correlations describing the heat transfer. Therefore, new formulae were developed (see Table 4) in the form:

$$Nu = ARe^B\mathrm{Pr}^{1/3}, \tag{9}$$

where *A* and *B* differ for meshes. The fit of the developed equations to the experimental data is presented in Figure 8.

Table 4. Correlations for Nusselt numbers of expanded metal meshes.

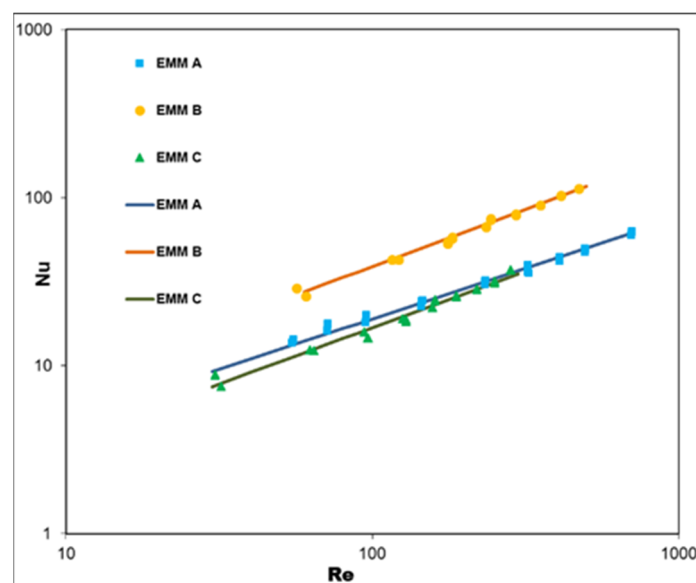| EMM	Correlation	Correlation Factor R^2	Difference [%]	No of Exp. Points
A	$Nu = 1.2Re^{0.6}\mathrm{Pr}^{1/3}$	0.9956	4.06	32
B	$Nu = 1.7Re^{0.68}\mathrm{Pr}^{1/3}$	0.9913	3.55	24
C	$Nu = 0.77Re^{0.67}\mathrm{Pr}^{1/3}$	0.9802	4.76	28

Figure 8. Comparison of Nusselt number derived from experiments (points) and calculated by correlations from Table 4 (lines).

3.3. Comparison of Different Catalyst Supports

The comparison of expanded metal meshes with other reactors' internals, such as the monolith, packed bed, or woven-wire gauze, is presented in Figure 9. The data on the specific surface area and void fraction of the compared packings are collated in Table 5.
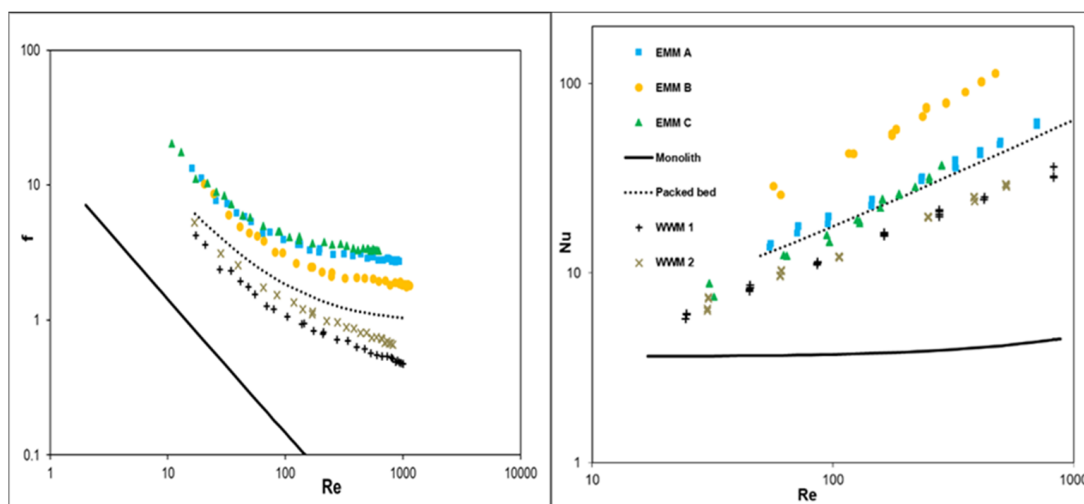

Figure 9. Comparison of flow resistance (**left**) and heat transfer (**right**) of different reactor packings.

Table 5. Comparison of expanded meshes with other catalyst carriers.

Support Type		S_v [m^2/m^3]	ε	D_h [mm]
	A	1100	0.84	3.05
EMM	B	900	0.9	4
	C	1700	0.84	1.98
WWM [29]	No. 1 (d = 5 mm)	1025	0.786	2.93
	No. 2 (d = 1.13 mm)	1252	0.754	2.52
Monolith (L = 0.2 m)		1339	0.72	2.15
Packed bed (D_p = 3 mm)		1220	0.39	1.28

As can be seen from Figure 9, expanded meshes display higher flow resistance than the packed bed, but also more intense heat transfer, especially EMM type B. The lowest values of Fanning friction factors and Nusselt numbers are achieved for the monolith. However, it is not clear which reactor's internal structure is the most efficient as a catalyst support. One of the meaningful ways to find the best solution for a given catalytic process is to use the Performance Efficiency Criterion (PEC) (Figure 10), which expresses the trade-off of the mass transfer intensity vs. the flow resistance [8,13]:

$$PEC = \frac{D_h S_v Sh}{2 f Re Sc \varepsilon}, \tag{10}$$

The air–methane mixture was the tested reaction [13]. The Chilton–Colburn analogy [30] was applied to calculate the mass transfer coefficients:

$$\frac{Sh}{Sc^{1/3}} = \frac{Nu}{Pr^{1/3}}, \tag{11}$$

Due to the highest PEC values, the monolith is the most beneficial catalyst support for the reaction mentioned. Although mesh type B indicates the highest flow resistance, its PEC values are comparable with that of wire gauzes because of the much more intense

heat transfer. Mesh types A and C are not suitable for methane combustion due to their high flow resistance and, hence, low PEC values.
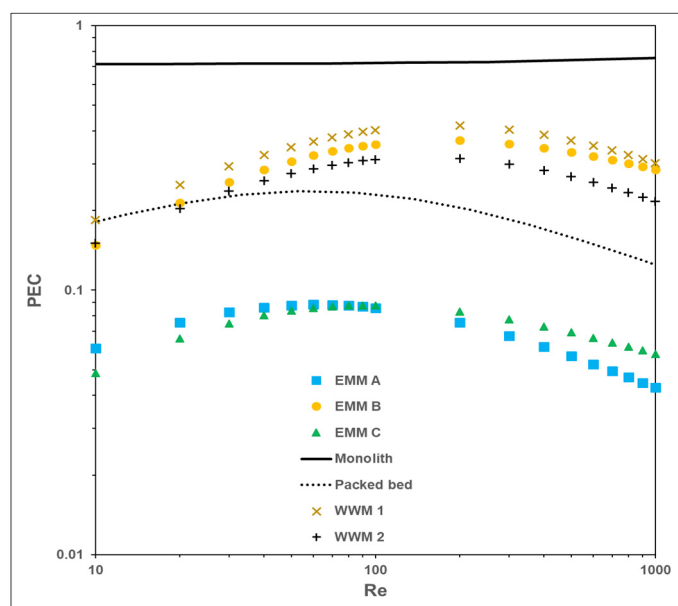

Figure 10. Comparison of Performance Efficiency Criterion of different reactor packings.

4. Conclusions

New formulae to evaluate the heat transfer and flow resistance characteristics of expanded metal meshes were developed. Fanning friction factors and Nusselt numbers were described by three equations dependent on the mesh type. The dimensions of meshes have an impact on the flow and transport characteristics; mesh type B seems to have the most desirable geometry.

Simple CFD models of expanded metal meshes were used to simulate the pressure drop and heat transfer coefficients. Numerical results agree well with experimental data. CFD modelling could be employed as a rapid and effective tool to predict the flow and transport properties of EMMs.

The comparison of expanded metal meshes with the monolith, packed bed, and woven-wire gauzes showed that their flow and transport characteristics are higher than other reactor internals. The Performance Efficiency Criterion (PEC) indicated that EMM type B and wire gauzes can be applied as catalyst carriers for methane oxidation.

Nomenclature

A, B	constants
c_p	specific heat, $J \cdot kg^{-1} \cdot K^{-1}$
D_p	grain diameter, mm
D_h	hydraulic diameter, mm
d	wire diameter, mm
e_y	average relative error, %
F	surface area, m^2
f	Fanning friction factor,
h	heat transfer coefficient, $W \cdot m^{-2} \cdot K^{-1}$
k	thermal conductivity, $W \cdot m^{-1} \cdot K^{-1}$
L	bed length, m
Nu	Nusselt number
ΔP	pressure drop, Pa
Pr	Prandtl number
p	static pressure, Pa
q	heat flux, $W \cdot m^{-2}$
Re	Reynolds number
S	sheet thickness, mm
Sc	Schmidt number
Sh	Sherwood number
S_v	specific surface area, $m^2 \cdot m^{-3}$
T	temperature, K
T	strand thickness, mm
u_i, u_j	velocity component
u_0	superficial (approach) velocity, $m \cdot s^{-1}$
W	strand width, mm
x_i, x_j	Cartesian coordinate
ε	porosity
μ	viscosity, Pa·s
ρ	density, $kg \cdot m^{-3}$
τ_{ij}	stress tensor

References

1. Tang, H.-Y.; Erickson, P.; Yoon, H.C.; Liao, C.-H. Comparison of steam and autothermal reforming of methanol using a packed-bed low-cost copper catalyst. *Int. J. Hydrogen Energy* **2009**, *34*, 7656–7665. [CrossRef]
2. Yang, J.; Wang, Q.; Zeng, M.; Nakayama, A. Computational study of forced convective heat transfer in structured packed beds with spherical or ellipsoidal particles. *Chem. Eng. Sci.* **2010**, *65*, 726–738. [CrossRef]
3. Kołodziej, A.; Łojewska, J.; Łojewski, T.; Iwaniszyn, M. Short-channel structures of triangular cross-section. *Int. J. Heat Mass Transf.* **2011**, *54*, 3291–3295. [CrossRef]
4. Kołodziej, A.; Łojewska, J.; Ochońska, J.; Łojewski, T. Short-channel structured reactor: Experiments versus previous theoretical design. *Chem. Eng. Process.-Process Intensif.* **2011**, *50*, 869–876. [CrossRef]
5. Iwaniszyn, M.; Ochońska, J.; Jodłowski, P.J.; Knapik, A.; Łojewska, J.; Janowska-Renkas, E.; Kołodziej, A. Short-channel structured reactor as a catalytic afterburner. *Top. Catal.* **2013**, *56*, 273–278. [CrossRef]
6. Iwaniszyn, M.; Ochońska, J.; Jodłowski, P.J.; Łojewska, J.; Matuszek-Chmurowska, A.; Kołodziej, A. Microstructured reactor as a pre-turbo catalytic converter. *Top. Catal.* **2013**, *56*, 384–389. [CrossRef]
7. Jodłowski, P.J.; Kryca, J.; Rogulska, A.; Gil, B.; Iwaniszyn, M.; Łojewska, J.; Kołodziej, A. New method of determination of intrinsic kinetic and mass transport parameters from typical catalyst activity tests: Problem of mass transfer resistance and diffusional limitation of reaction rate. *Chem. Eng. J.* **2017**, *162*, 322–331. [CrossRef]
8. Giani, L.; Groppi, G.; Tronconi, E. Mass-Transfer Characterization of Metallic Foams as Supports for Structured Catalysts. *Ind. Eng. Chem. Res.* **2005**, *44*, 4993–5002. [CrossRef]
9. Peng, W.; Xu, M.; Li, X.; Huai, X.; Liu, Z.; Wang, H. CFD study on thermal transport in open-cell metal foams with and without a washcoat: Effective thermal conductivity and gas-solid interfacial heat transfer. *Chem. Eng. Sci.* **2017**, *161*, 92–108. [CrossRef]
10. Bianchi, G.; Schwieger, W.; Freund, H. Assessment of Periodic Open Cellular Structures for Enhanced Heat conduction in Catalytic Fixed-Bed Reactors. *Adv. Eng. Mater.* **2016**, *18*, 608–614. [CrossRef]
11. Kumar, P.; Topin, F. Simultaneous determination of intrinsic solid phase conductivity and effective thermal conductivity of Kelvin like foams. *Appl. Therm. Eng.* **2014**, *71*, 536–547. [CrossRef]

12. Bracconi, M.; Ambrosetti, M.; Maestri, M.; Groppi, G.; Tronconi, E. A systematic procedure for the virtual reconstruction of open-cell foams. *Chem. Eng. J.* **2017**, *315*, 608–620. [CrossRef]

13. Gancarczyk, A.; Iwaniszyn, M.; Piątek, M.; Korpyś, M.; Sindera, K.; Jodłowski, P.J.; Łojewska, J.; Kołodziej, A. Catalytic Combustion of Low-Concentration methane on Structured Catalyst Supports. *Ind. Eng. Chem. Res.* **2018**, *57*, 10281–10291. [CrossRef]

14. Busse, C.; Freud, H.; Schwieger, W. Intensification of heat transfer in catalytic reactors by additively manufactured periodic open cellular structures (POCS). *Chem. Eng. Process.-Process Intensif.* **2018**, *124*, 199–214. [CrossRef]

15. Klumpp, M.; Inayat, A.; Schwerdtfeger, J.; Korner, C.; Singer, R.F.; Freund, H.; Schwieger, W. Periodic open cellular structures with ideal cubic cell geometry: Effect of porosity and cell orientation on pressure drop behavior. *Chem. Eng. J.* **2014**, *242*, 364–378. [CrossRef]

16. Oshinowo, L.; Kuhn, D.C.S. Turbulence Decay Behind Expanded Metal Screens. *Can. J. Chem. Eng.* **2000**, *78*, 1032–1039. [CrossRef]

17. Smith, D.; Graciano, C.; Martínez, G. Expanded metal: A review of manufacturing, applications and structural performance. *Thin-Walled Struct.* **2021**, *160*, 107371. [CrossRef]

18. Kołodziej, A.; Łojewska, J. Mass transfer for woven and knitted wire gauze substrates: Experiments and modelling. *Catal. Today* **2009**, *147S*, S120–S124. [CrossRef]

19. Ahlström-Silversand, A.F.; Odenbrand, C.U.I. Modelling catalytic combustion of carbon monoxide and hydrocarbons over catalytically active wire meshes. *Chem. Eng. J.* **1999**, *73*, 205–216. [CrossRef]

20. Lyubovsky, M.; Karim, H.; Menacherry, P.; Boorse, S.; LaPierre, R.; Pfefferle, W.C.; Roychoudhury, S. Complete and partial catalytic oxidation of methane over substrates with enhanced transport properties. *Catal. Today* **2003**, *83*, 183–197. [CrossRef]

21. Porsin, A.V.; Kulikov, A.V.; Dalyuk, I.K.; Rogozhnikov, V.N.; Kochergin, V.I. Catalytic reactor with metal gauze catalysts for combustion of liquid fuel. *Chem. Eng. J.* **2015**, *282*, 233–240. [CrossRef]

22. Jodłowski, P.J.; Kuterasiński, Ł.; Jędrzejczyk, R.J.; Chlebda, D.; Gancarczyk, A.; Basąg, S.; Chmielarz, Ł. DeNOx Abatement Modelling over Sonically Prepared Copper USY and ZSM5 Structured Catalysts. *Catalysts* **2017**, *7*, 205. [CrossRef]

23. Zalosh, R. Deflagration suppression using expanded metal mesh and polymer foams. *J. Loss Prev. Process Ind.* **2007**, *20*, 659–663. [CrossRef]

24. Mustaffar, A.; Harvey, A.; Reay, D. Melting of phase change material assisted by expanded metal mesh. *Appl. Therm. Eng.* **2015**, *90*, 1052–1060. [CrossRef]

25. Lafmejani, S.S.; Müller, M.; Olesen, A.C.; Kær, S.K. Experimental and numerical study of flow in expanded metal plate for water electrolysis applications. *J. Power Sources* **2018**, *397*, 334–342. [CrossRef]

26. Saini, R.P.; Saini, J.S. Heat transfer and friction factor correlations for artificially roughened ducts with expanded metal mesh as roughness element. *Int. J. Heat Mass Transf.* **1997**, *40*, 973–986. [CrossRef]

27. Mallick, R.K.; Thombre, S.B. Performance of passive DMFC with expanded metal mesh current collectors. *Electrochim. Acta* **2017**, *243*, 299–309. [CrossRef]

28. Ergun, S. Fluid flow through packed columns. *Chem. Eng. Prog.* **1952**, *48*, 89–94.

29. Iwaniszyn, M.; Sindera, K.; Gancarczyk, A.; Korpyś, M.; Jędrzejczyk, R.J.; Kołodziej, A.; Jodłowski, P.J. Experimental and CFD investigation of heat transfer and flow resistance in woven wire gauzes. *Chem. Eng. Process.-Process Intensif.* **2021**, *163*, 108364. [CrossRef]

30. Chilton, T.H.; Colburn, A.P. Mass transfer (absorption) coefficients prediction from data on heat transfer and fluid friction. *Ind. Eng. Chem.* **1934**, *26*, 1183–1187. [CrossRef]